Northumbria Research Link

Northumbria University
NEWCASTLE

UniversityLibrary

Polyhedral Carbon Anchored on Carbon Nanosheet with Abundant Atomic Fe-N$_x$ Moieties for Oxygen Reduction

Dong Liu, Chenxi Huyan, Yuanyuan Zhao, Terence Xiaoteng Liu, Ding Wang, Jining Sun, Sheng Dai, Fei Chen, and Ben Bin Xu*

Carbon-based single-atom iron electrocatalysts with nitrogen coordination (CSAIN) have recently shown enormous promise to replace the costly Pt for boosting the cathodic oxygen reduction reaction (ORR) in fuel cells. However, there remains a great challenge to achieve highly efficient CSAIN catalysts for the ORR in acidic electrolytes. Herein, a novel CSAIN catalyst is synthesized by pyrolyzing a precursor mixture consisting of metal–organic framework and conductive polymer hybrid. After pyrolysis at a high temperature, the CSAIN with a structure of carbon nanosheet supported polyhedral carbon is achieved, where the unique structure endows CSAIN with expediting electron transfer and mass transport, as well as largely exposed surface to host atomically dispersed iron active sites. As a result, the optimal CSAIN catalyst shows a high ORR activity with its half-wave potential of 0.77 V (vs RHE) and a Tafel slope of 74.1 mV dec^{-1}, which are comparable to that of commercial Pt/C catalyst (0.80 V and 81.9 mV dec^{-1}).

1. Introduction

The electrochemical oxygen reduction reaction (ORR) holds great promises in emerging electrochemical energy application, such as proton exchange membrane fuel cells (PEMFC), to tackle the urgent challenges in the sector of clean and renewable energy (i.e., Net Zero).[1–3] However, the inherited sluggish kinetics of ORR seriously constrains the further development of PEMFC. To boost the output performance of PEMFC, high-performance ORR electrocatalysts are a prerequisite. Noble metal Pt-based catalysts are recognized as one of the most efficient candidates for accelerating the ORR.[4,5] However, the Pt-based catalyst possess disadvantages as high cost, scarcity, low stability, and poor methanol tolerance, which seriously hinder their application.[6] Motivated by the above, considerable efforts have been paid for exploring inexpensive and highly efficient nonprecious metal catalysts (NPMC) to take the place of the Pt-based catalyst for the ORR.[7–11]

Pyrolyzed iron- and nitrogen-doped (Fe-N-C) materials are a group of NPMC with huge potential to replace the Pt-based catalyst for their maximum metal atom utilization and high exposure of active sites, which could yield favorable ORR performance. The active sites of Fe-N-C materials are made by the single iron atoms coordinated by nitrogen doping (Fe-N$_x$ moieties). Ding et al. reported an ion-imprinting derived strategy to develop carbon-based single-atom iron electrocatalysts with nitrogen coordination (CSAIN) with high concentrations of Fe-N$_4$ active sites, with a clear verification of the working mechanism of Fe-N$_4$ moieties during ORR process.[12] Whereas the synthesis of Fe-N-C materials is widely exercised by pyrolyzing the precursors containing iron, nitrogen, and carbon sources, technical challenges such as the low density of Fe-N$_x$ moieties and undesired ORR performance induced by the iron atoms agglomeration remain to be overcome.[13–15]

Zeolitic-imidazolate type of metal-organic framework with coordination Zinc atoms (ZIF-8) has been frequently used in

D. Liu, C. Huyan, Y. Zhao, F. Chen
School of Chemical Engineering and Technology
Xi'an Jiaotong University
Xi'an 710049, P. R. China

Y. Zhao
The 41st Institute of the Forth Academy
China Aerospace Science and Technology Corporation
Xi'an, Shaanxi 710025, P. R. China

T. X. Liu, B. B. Xu
Mechanical and Construction Engineering
Faculty of Engineering and Environment
Northumbria University
Newcastle upon Tyne NE1 8ST, UK
E-mail: ben.xu@northumbria.ac.uk

D. Wang
Faculty of Engineering and Physical Sciences
University of Southampton
University Road, Southampton SO17 1BJ, UK

J. Sun
School of Mechanical Engineering
Dalian University of Technology
Dalian 116024, P. R. China

S. Dai
School of Chemical and Process Engineering
University of Leeds
Leeds LS2 9JT, UK

preparing precursors of Fe-N-C catalysts,[16] since the coordination structure of ZIF-8 (Zn-N$_4$) is similar to that of Fe-N$_x$ active site. ZIF-8 also possesses excellent configurability on the structure by substituting the Zinc center with other ions.[17] When the Zinc atoms in ZIF-8 are substituted by iron atoms or encapsulated into the void of ZIF-8, iron-modified ZIF-8 (Fe-ZIF8) precursors can be achieved. By subsequently pyrolyzing at high temperature, the iron atoms will be directly converted into active Fe-N$_x$ moieties. Since the Fe-ZIF8 derived Fe-N-C materials are independent of each other, the charge transfer is mainly dependent on the physical stacking of nanoparticles during the ORR process, resulting in an unideal charge transfer pathway.[18] Recently, conductive carbon nanomaterials have been utilized as linkers to connect ZIF nanoparticles, enabling an enhanced charge transfer speed and improved electrochemical performance.[19,20] However, the exposed surface of conductive carbon nanomaterials is inactive due to the absence of active sites, which will lead to a compromise in the electrocatalytic performance.

Herein, we developed a novel polyhedral carbon anchored on carbon nanosheet (PCCNS) strategy with abundant Fe-N$_x$ moieties. Fe-N-doped carbon nanosheet, originated from graphene oxide supported iron-modified polypyrrole, acts as a linker to connect ZIF-derived polyhedral Fe-N-C particles. Aberration-corrected transmission electron microscopy (TEM) and X-ray absorption spectroscopy (XAS) characterizations confirm the existence of iron with the state of atomically dispersed Fe-N$_x$ moieties in the final catalyst. Benefit from the unique structure, the final catalytical material shows excellent ORR performance in an acidic condition with an onset potential of 0.87 V and half-wave potential of 0.77 V versus RHE, which is comparable to commercial Pt/C catalyst (0.91 and 0.80 V). Meanwhile, the PCCNS-20 catalyst expressed lower Tafel slope of 74.1 mV dec^{-1} than that of Pt/C (81.9 mV dec^{-1}).

2. Results and Discussion

The synthesis of PCCNS catalyst is diagrammatically illustrated in **Figure 1**. The key to the above process is to absorb Fe^{3+} and Zn^{2+} on the polypyrrole-coated graphene oxide (PPy@GO) that act as the "seeds" to grow Fe-ZIF8, therefore leading to a solid connection between PPy@GO and Fe-ZIF8.
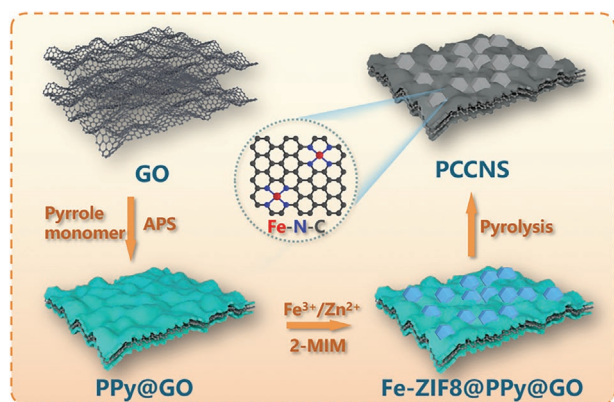

Figure 1. Schematic illustration of the synthesis process of the PCCNS catalysts.

In **Figure 2**a, the SEM clearly proves that the Fe-ZIF8 has been successfully grown on the surface of PPy@GO sheets, forming the Fe-ZIF8@PPy@GO nanocomposite (Figure S1, Supporting Information). Meanwhile, the PPy and Fe-ZIF8 act as steric barriers to reduce the aggregation of 2D PPy@GO nanosheet.[21] After carbonizing at 900 °C, we observe the obtained PCCNS catalyst under TEM(Figure S2, Supporting Information), found that the Fe-ZIF8 derived polyhedral carbon has been grafted on the Fe-N-doped carbon nanosheet tightly. The polyhedral carbon inherited the rhombic dodecahedral nanostructure from the previous state (Figure 2b), and small deformations and collapses are observed owing to the evaporation of Zn atoms. From the energy-dispersive X-ray spectroscopy (EDS) analysis of PCCNS-20 (Figure 2c and Figure S3, Supporting Information), a uniform distribution of C, N, O, Fe, and Zn atoms in the carbon matrix are found with the TEM view on the whole area (Figure 2c inset). Notably, no iron is detected since the Fe disperse at an atomic level. The presence of Zn in PCCNS catalyst proves that some Zn atoms residues during the carbonizing process. Moreover, the high-angle annular dark-field scanning TEM(HAADF-STEM) results (Figure 1d), reveal no trace of Fe as the Fe–N$_x$ centers are encapsulated with carbon.

The X-ray absorption fine structure (XAFS) technique was conducted to investigate the structure of Fe species in PCCNS-20. Fe K-edge X-ray absorption near-edge spectroscopy (XANES) curves of PCCNS-20 with FeO, Fe foil, and Fe$_2$O$_3$ references are shown in **Figure 3**a. The absorption threshold curve of PCCNS-20 located between FeO and Fe$_2$O$_3$ indicates that the Fe valence is situated between Fe^{2+} and Fe^{3+}.[22] Fourier transform (FT) EXAFS (Figure 3b) reveals that PCCNS-20 has a main peak centered at ≈ 1.5 Å, which assigns to the Fe-N scattering path, indicating the successful isolation of Fe atoms.[5]

We also perform the wavelet transform (WT) of the Fe K-edge EXAFS oscillations to further understand the atomic dispersion of Fe atoms over the entire architecture of PCCNS-20. In Figure 3c, it can be found that one WT maximum at ≈ 4.5 Å^{-1}, which was originated from Fe-N bonding. Figure S4 (Supporting Information) shows the Raman spectra of PCCNS catalyst. All the curves exhibited typical amorphous carbon with the two representative bands: D band located at 1350 cm^{-1} assigned to lattice defect and G band located at 1580 cm^{-1} corresponds to the sp2 hybridized carbon atoms, respectively.[23] There was no obvious difference among the I_D/I_G ratio of all PCCNS catalysts, revealing that the Fe^{3+} has little effect on graphitization. The surface area is another key feature to influence the ORR performance. The nitrogen adsorption-desorption isotherm curve of PCCNS-20 (Figure S5, Supporting Information) presents a typical type-IV isotherm with an obvious hysteresis loop at the relative pressure range of 0.4–1, corresponding to the specific mesopores structure. Besides, the sharp increase at relatively low pressure corresponded to the presence of micropores.[24] The Brunauer–Emmett–Teller (BET) surface area of PCCNS-20 catalyst was calculated to be 447.8 cm^2 g^{-1}. The pore size is estimated through the Barrett–Joyner–Halenda (BJH) method and the results show a distribution between the micropores with an average size of 1.7 nm and mesopores with an average diameter of 3.8 nm (Figure S5, Supporting Information inset).
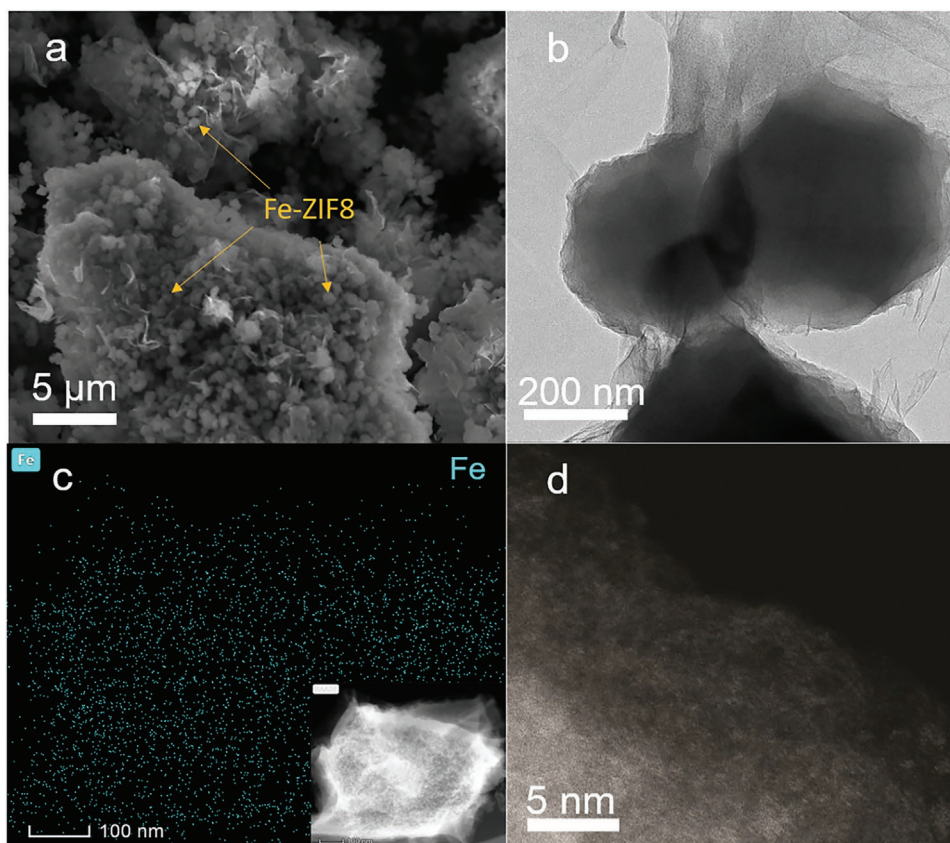
Figure 2. a) SEM image of Fe-ZIF8 coated on PPy@GO; b) TEM images of PCCNS-20; c) elemental mapping photo of Fe atoms in PCCNS-20; inset is the STEM of the corresponding area; d) HAADF-STEM image of PCCNS-20.

We further study the structure of PCCNS catalyst with different feeding ratios of Fe^{3+}, by performing the X-ray photoelectron spectroscopy (XPS) tests for PCCNS-10, PCCNS-20, and PCCNS-30 (Figure S6, Supporting Information). All spectra present C, N, O, Fe, and Zn peaks, consistent with the EDS mapping. The XPS results for bulk nitrogen and iron contents of PCCNS catalysts are listed in **Table 1**. Interestingly, the PCCNS-20 possess both the highest nitrogen content and

iron content of ≈5.83 and 0.39 at%, meeting the merit for a higher ORR activity. PCCNS-30 presents lower Fe content than PCCNS-20, as its higher content Fe atoms in precursor intend to aggregate to Fe clusters during pyrolysis and Fe clusters seem to be encapsulated in graphite carbon, which makes it hard to be detected by XPS.

Figure 4a exhibits the high-resolution of N 1s XPS spectra of PCCNS-10, PCCNS-20, and PCCNS-30. We deconvolute the
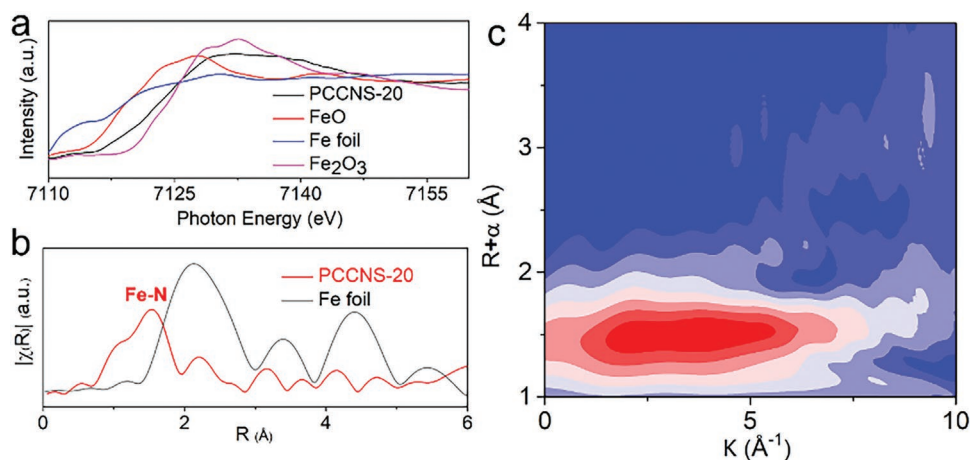

Figure 3. a) Normalized XANES spectra of Fe K-edge with different adsorption energy for PCCNS-20, FeO, Fe foil, and Fe_2O_3, respectively; b) FT-EXAFS spectra at the K-edge for PCCNS-20 and Fe foil; c) WT spectrum of PCCNS-20.

ADVANCED
SCIENCE NEWS
www.advancedsciencenews.com

ADVANCED
MATERIALS
INTERFACES
www.advmatinterfaces.de

Table 1. The Fe and N atoms content in PCCNS catalysts detective by XPS.

	PCCNS-10	PCCNS-20	PCCNS-30
Fe [at.%]	0.28	0.39	0.36
N [at.%]	5.47	5.83	3.91

N 1s peak into four peaks at 398.6, 400.0, 401.1, and 402.5 eV, which are assigned to pyridinic-N, pyrrole-N, graphitic-N, and oxidized-N (N-O) based on the respective binding energy.[25,26] In Figure 4b, the PCCNS-20 exhibited the highest content of pyridinic N (62.1%) than that of PCCNS-10 (43.1%) and PCCNS-30 (38.3%). The pyridinic N species possess a long pair of electrons and tend to coordinate Fe^{3+} to construct $Fe-N_x$ sites, which serve as the catalytically active center to promote the ORR performance in the acidic solution.[27,28] The high-resolution C1s spectrum (Figure S7, Supporting Information) of PCCNS-20 can be divided into three peaks with one strong peak and two weak peaks located at binding energies of 284.5, 285.1, and 285.9 eV, corresponding to the Sp^2 C—N, Sp^3 C—N, and C=O/C=N center,[29,30] respectively. Figure 4c shows the high-resolution spectrum Fe 2p of PCCNS-20, the main peak can be fitted into five peaks at 709.3, 712.4, 716.5, 723.2, and 726.8 eV. The peaks at binding energies of 709.3 and 712.4 eV were assigned to the Fe^{2+} and Fe^{3+} of $2p_{3/2}$, while the peaks located at 723.2 and 726.8 eV corresponded to the Fe^{2+} and Fe^{3+} of $2p_{1/2}$. The above four peaks indicate that Fe coordinates with N atom to form the $Fe^{2+/3+}-N_x$ moieties, in a good agreement with the previous reports.[31–33] Thus, the Fe atoms are atomically dispersed in the product.

We then assess the ORR electrocatalytic activity of PCCNS catalysts, with a loading density of 0.2 mg cm^{-2} in 0.1 M $HClO_4$ solution based on the rotating disk electrode (RDE). The commercial Pt/C (20%; 0.2 mg cm^{-2}) is utilized in the same setting for comparison. Figure S8 (Supporting Information) shows the cyclic voltammetry (CV) curves of PCCNS catalysts under a scan rate of 10 mV s^{-1} with 1600 rpm rotation speed. All the three curves present quasi-rectangular shaped double-layer capacity current, obvious cathodic peaks located at about 0.66 V versus RHE in the oxygen saturated solution, as well as symmetric anodic peaks located at 0.82 V, demonstrating the redox reaction occurred between Fe^{2+} and Fe^{3+},[25] favorable for the catalytic ORR activity. The steady-state linear sweep voltammetry (LSV) is utilized to evaluate the ORR activities of as-obtained PCCNS catalysts (**Figure 5**a), the onset potential (E_0), and half-wave potential ($E_{1/2}$) of PCCNS and Pt/C catalysts are shown in Figure S9 (Supporting Information). The PCCNS-20 present relatively higher E_0 (0.87 V vs RHE) and $E_{1/2}$ (0.77 V vs RHE) than others, with a marginal lower than commercial Pt/C, comparable to the decent Fe-N-C reports[23,34–37] (**Table 2**).

On the one hand, PCCNS-10 catalyst presents the most negative E_0 and $E_{1/2}$, due to the low density of $Fe-N_x$ species, which plays a critical role in the electron-transfer process. On the other hand, the ORR activity decreases when we increase the feeding ratio of Fe^{3+} to 30 mg, the little lower E_0 and $E_{1/2}$ of PCCNS-30 than PCCNS-20 which is caused by the aggregation of redundant Fe during the pyrolysis. The Fe clusters that can be detected from TEM and XRD (Figures S10 and S11, supporting information) limit the ORR active performance of the PCCNS-30 catalyst. Notably, the PCCNS-10, PCCNS-20, and PCCNS-30 possess large limiting current density (j_L) of
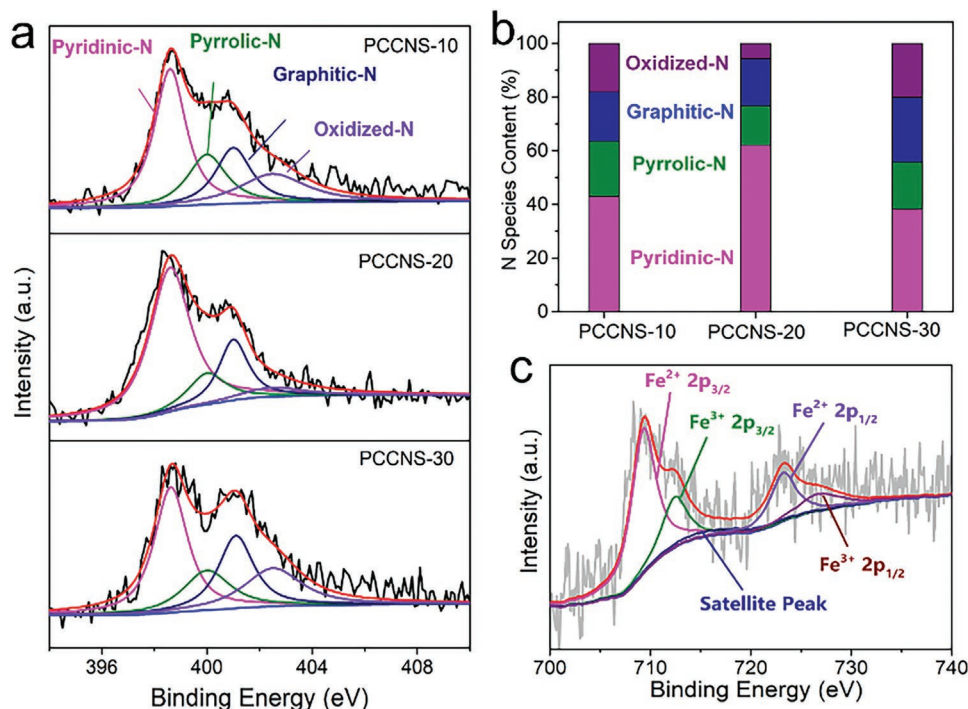

Figure 4. a) N1s spectra of PCCNS catalysts; b) The content of different types of nitrogen in the PCCNS catalysts; c) Fe 2p curve of the PCCNS-20.
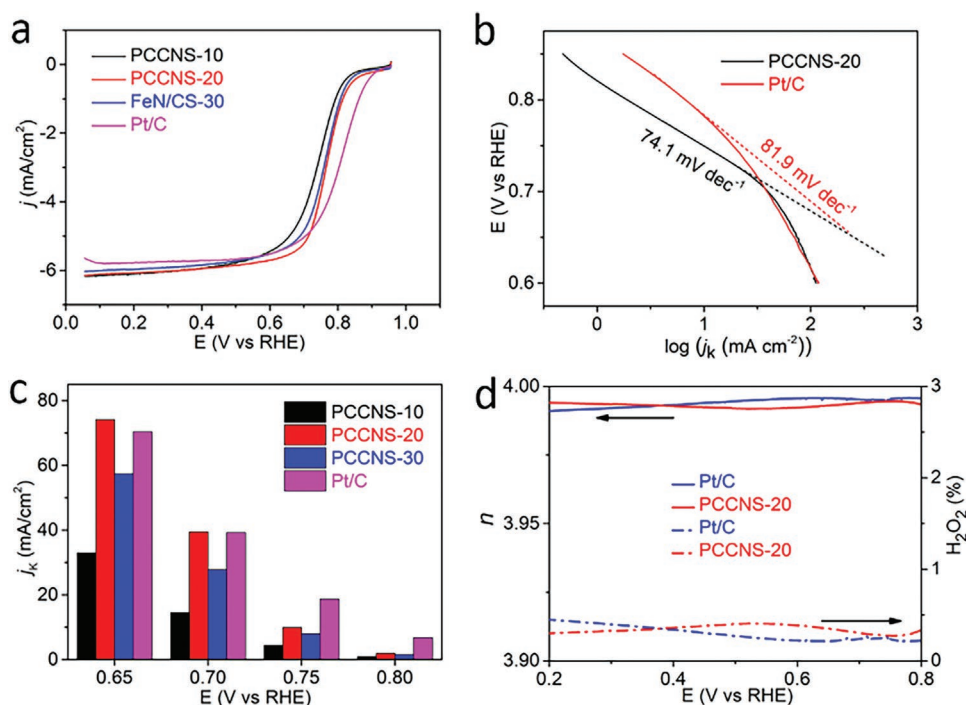
Figure 5. a) RDE polarization curves at 1600 rpm for PCCNS and commercial Pt/C catalysts; b) Tafel plots of PCCNS-20 and Pt/C catalysts; c) kinetic current densities of the PCCNS and Pt/C catalysts at the potential range of 0.65–0.8 V; d) electron transfer number (top) and hydrogen peroxide species yield (bottom) of PCCNS-20 and Pt/C.

≈6.0 mA cm^{-2}, superior to Pt/C (5.8 mA cm^{-2}), indicating the highly efficient mass transport pathway.

We next study the ORR kinetics character between PCCNS-20 and Pt/C by summarizing the Tafel plots of the polarization curves in Figure 5b. The Tafel slope of PCCNS-20 (74.1 mV dec^{-1}) seems much lower than that of Pt/C (81.9 mV dec^{-1}). The lower Tafel slope of PCCNS-20 demonstrates that the first electron transfer way tends to be the rate-determining step during the catalyst process.[38,39] We calculate the kinetic current densities (j_k) of PCCNS-10, PCCNS-20, PCCNS-30, and Pt/C under the potential range of 0.65–0.8 V (Figure 5c). The PCCNS-20 exhibits the largest j_k value among all PCCNS catalysts, which is at the same level as the commercial Pt/C. These results indicate that PCCNS-20 has the highest active site volumetric density and strong mass/charge transport capability.[40] We further analyzed the rotating ring-disk electrode (RRDE) results to calculate the electron transfer number (n) and the peroxide species yield (H$_2$O$_2$%). In Figure 5d, the n value of the PCCNS-20 is identified between 3.98 and 4.00 at the potential range of 0.2–0.8 V, almost the same as the commercial Pt/C. This demonstrates the highly efficient oxygen reduction process in the PCCNS-20 catalytic system followed the nearly constant 4 electron pathway. Both the yield of H$_2$O$_2$ of PCCNS-20 and Pt/C are less than 1%, benefiting from the high ORR.

We further assess the charge transfer speed of PCCNS-20 and Fe-ZIF8 derived carbon cluster synthesized by the same procedure of PCCNS catalyst but without adding GO and PANI, by performing the electrochemical impedance spectroscopy (EIS) analyses of them in 0.1 M HClO$_4$ solution from 10^5 Hz to 10^{-1} Hz. As shown in Figure S12 (Supporting Information), both smaller arc and real-axis intercept in the PCCNS-20 curve could be observed in high-frequency region, suggesting lower interfacial charge-transfer resistance (R$_S$) and bulk-electrolyte solution resistance (R$_{CT}$). The reason is that the PCCNS-20 catalyst has higher electrical conductivity by linking the isolated carbon cluster together. The stability measurement of PCCNS-20 and Pt/C catalyst in an acidic environment were also conducted by the continuously chronoamperometric measurement with a rotation rate of 1600 rpm. It is found that PCCNS-20 exhibit lower current decay (Figure S13, Supporting Information) than Pt/C in acidic electrolyte, indicating its superior ORR stability.

The above catalytic performance of PCCNS-20 has demonstrated attractive application potentials with features that is comparable to that of commercial Pt/C. The underlying mechanism can be summarized with the following points: (1) Fe and Zn atoms can be easily embedded into PPy@GO matrix to construct Fe-ZIF8@PPy@GO precursor. The Fe atoms can enhance the Fe-N$_x$ active center by either substituting the Zn atoms in ZIF-8 or inserting into PPy to cooperate with nitrogen

Table 2. Comparison of E_0, $E_{1/2}$ and Tafel slope values of PCCNS-20 with published state-of-the-art Fe-N-C catalysts.

	E_0 (V vs RHE)	$E_{1/2}$ (V vs RHE)	Tafel slop [mV dec^{-1}]
Fe-N-C (S) catalyst[22]	0.83	0.71	–
Co, Fe SAs/NC[33]	0.86	0.75	86
Fe-N-C/N-OMC[34]	0.91	0.73	76
Fe-N-C/H$_2$O$_2$[35]	0.93	0.79	85.3
230-002-C30[36]	–	0.76	88
PCCNS-20[this work]	0.87	0.77	74.1

ADVANCED
SCIENCE NEWS
www.advancedsciencenews.com

ADVANCED
MATERIALS
INTERFACES
www.advmatinterfaces.de

atoms, with the Zn atoms acting as the separator to prevent the Fe atom from aggregation during carbonization. (2) High percentage of pyridinic typed N ensures the N atoms to cooperate effectively with uniformly dispersed Fe atoms to build the Fe-N_x active center, to promote the ORR activity. (3) The designable Fe-N-doped carbon nanosheet endows a tight connection between polyhedral carbon, offering high ways for charge/mass transfer and a higher electron transfer speed, yield a favorable ORR activity.

3. Conclusion

In this work, we have developed a highly efficient polyhedral carbon anchored carbon nanosheet electrocatalyst with atomic Fe-N_x moiety dispersed in an acidic medium. Results show that the feeding content of Fe^{3+} can affect the ORR activity of catalysts, the optimal PCCNS-20 catalyst exhibits the highest ORR performance comparable to that of commercial Pt/C. The PCCNS-20 showed high ORR activity with an E_0 of 0.87 V and $E_{1/2}$ of 0.77 V versus RHE. Meanwhile, the PCCNS-20 catalyst expressed a lower Tafel slope of 74.1 mV dec^{-1} than that of Pt/C (81.9 mV dec^{-1}). The further study on the performance of PCCNS-20 catalyst in acidic electrolyte, indicates a designed continuous structure enabled high mass transfer speed for ORR with an efficient four-electron-transfer pathway. Given the promising results, we expect the PCCNS-20 catalyst to find potential applications to replace the traditional materials in PEMFCs with superior ORR performance in acidic media.

4. Experimental Section

Materials and Reagents: GO was purchased from Shenzhen Matterene Technology Co. Ltd. Pyrrole monomer (99%) was obtained from Shanghai Adamas Regent Co. Ltd. Ammonium persulfate (APS, A.R.) and 2-methylimidazole (2-MIM, 98%) were obtained from Shanghai Macklin Biochemical Co. Ltd. $Fe(NO_3)_3 \cdot 9H_2O$ (A.R.) and $Zn(NO_3)_2 \cdot 6H_2O$ (A.R.) were purchased from Shanghai Aladdin Biochemical Technology Co. Ltd. Deionized (DI) water was used throughout the experimental procedure.

Synthesis of PPy@GO Nanosheet: The purchased GO was first dissolved in the DI water under sonication for 1 h. Then 0.5 mL pyrrole monomer was added into 50 mL 2 mg mL^{-1} GO solution to prepare pyrrole anchored GO solution. The PPy was in situ redox polymerized with APS (mole ratio of pyrrole monomer to APS is 1:1) acted as the oxidant. After washing with ethanol and DI water, the PPy@GO nanosheet was prepared.

Synthesis of Fe-ZIF8/PPy@GO: One gram PPy@GO nanosheet was dispersed into 100 mL methanol which contained 0.8 g $Zn(NO_3)_2 \cdot 6H_2O$ and a certain amount of $Fe(NO_3)_3 \cdot 9H_2O$, and kept stirring for 12 h to allow PPy@GO nanosheet fully adsorb Zn^{2+} and Fe^{3+}. 2-MIM (1.6 g) was added and the mixture was kept stirring for 6 h to grow the Fe-ZIF8 on the surface of PPy@GO nanosheet. The Fe-ZIF8 coated PPy@GO nanosheet was collected after centrifugation, washing with methanol five times and drying.

Synthesis of PCCNS Catalysts: Five hundred milligrams of as-prepared Fe-ZIF8/PPy@GO was carbonized by tube furnace under 900 °C with a heating rate of 5 °C min^{-1} at nitrogen atmosphere for 1 h. After cooling to room temperature, the product was acidic etched with 0.5 M H_2SO_4 under 80 °C for 6 h to remove the Fe cluster aggregated in pyrolyzed process. The PCCNS catalyst was successfully synthesized after washing and vacuum drying. For comparison, the PCCNS-X were denoted to be the production with adding various amounts of $Fe(NO_3)_3 \cdot 9H_2O$

(X means the feeding mass of $Fe(NO_3)_3 \cdot 9H_2O$). For example, PCCNS-10 means adding 10 mg $Fe(NO_3)_3 \cdot 9H_2O$ during the synthesis process.

Conflict of Interest

The authors declare no conflict of interest.

Data Availability Statement

The data that support the findings of this study are available in the supplementary material of this article.

[1] B. Y. Xia, Y. Yan, N. Li, H. B. Wu, X. W. Lou, X. Wang, *Nat. Energy* **2016**, *1*, 15006.
[2] M. Shao, Q. Chang, J. P. Dodelet, R. Chenitz, *Chem. Rev.* **2016**, *116*, 3594.
[3] A. Kulkarni, S. Siahrostami, A. Patel, J. K. Norskov, *Chem. Rev.* **2018**, *118*, 2302.
[4] A. Zadick, L. Dubau, N. Sergent, G. Berthomé, M. Chatenet, *ACS Catal.* **2015**, *5*, 4819.
[5] Y. Lin, P. Liu, E. Velasco, G. Yao, Z. Tian, L. Zhang, L. Chen, *Adv. Mater.* **2019**, *31*, 1808193.
[6] Y. Wang, H. Lei, S. Lu, Z. Yang, B. B. Xu, L. Xing, T. X. Liu, *Appl. Catal. B* **2022**, *305*, 121022.
[7] S. Kabir, S. Medina, G. Wang, G. Bender, S. Pylypenko, K. C. Neyerlin, *Nano Energy* **2020**, *73*.
[8] R. Wang, T. Yan, L. Han, G. Chen, H. Li, J. Zhang, L.-Y. Shi, D. Zhang, *J. Mater. Chem. A* **2018**, *6*, 5752.
[9] S. Fu, C. Zhu, J. Song, D. Du, Y. Lin, *Adv. Energy Mater.* **2017**, *7*, 1700363.
[10] J. C. Li, X. Qin, F. Xiao, C. Liang, M. Xu, Y. Meng, E. Sarnello, L. Fang, T. Li, S. Ding, Z. Lyu, S. Zhu, X. Pan, P. X. Hou, C. Liu, Y. Lin, M. Shao, *Nano Lett.* **2021**, *21*, 4508.
[11] X.-H. Yan, Z. Meng, P. Prabhu, H. Xu, T. Xue, G. Fang, J.-M. Lee, *Ind. Eng. Chem. Res.* **2020**, *59*, 3016.
[12] S. Ding, Z. Lyu, H. Zhong, D. Liu, E. Sarnello, L. Fang, M. Xu, M. H. Engelhard, H. Tian, T. Li, X. Pan, S. P. Beckman, S. Feng, D. Du, J. C. Li, M. Shao, Y. Lin, *Small* **2021**, *17*, e2004454.

[13] M. Chen, Y. He, J. S. Spendelow, G. Wu, *ACS Energy Lett.* **2019**, *4*, 1619.

[14] G. A. Ferrero, K. Preuss, A. Marinovic, A. B. Jorge, N. Mansor, D. J. Brett, A. B. Fuertes, M. Sevilla, M. M. Titirici, *ACS Nano* **2016**, *10*, 5922.

[15] J.-C. Li, F. Xiao, H. Zhong, T. Li, M. Xu, L. Ma, M. Cheng, D. Liu, S. Feng, Q. Shi, H.-M. Cheng, C. Liu, D. Du, S. P. Beckman, X. Pan, Y. Lin, M. Shao, *ACS Catal.* **2019**, *9*, 5929.

[16] J. Yan, X. Zheng, C. Wei, Z. Sun, K. Zeng, L. Shen, J. Sun, M. H. Rümmeli, R. Yang, *Carbon* **2021**, *171*, 320.

[17] P. Miao, K. Cheng, H. Li, J. Gu, K. Chen, S. Wang, D. Wang, T. X. Liu, B. B. Xu, J. Kong, *ACS Appl. Mater. Interfaces* **2019**, *11*, 17706.

[18] D. Liu, J. C. Li, S. Ding, Z. Lyu, S. Feng, H. Tian, C. Huyan, M. Xu, T. Li, D. Du, P. Liu, M. Shao, Y. Lin, *Small Methods* **2020**, *4*, 1900827.

[19] J. Wei, Y. Hu, Y. Liang, B. Kong, Z. Zheng, J. Zhang, S. P. Jiang, Y. Zhao, H. Wang, *J. Mater. Chem. A* **2017**, *5*, 10182.

[20] L. Ma, S. Chen, Z. Pei, Y. Huang, G. Liang, F. Mo, Q. Yang, J. Su, Y. Gao, J. A. Zapien, C. Zhi, *ACS Nano* **2018**, *12*, 1949.

[21] D. Liu, J. Liu, Q. Wang, P. Du, W. Wei, P. Liu, *Carbon* **2019**, *143*, 147.

[22] A. Zitolo, V. Goellner, V. Armel, M. T. Sougrati, T. Mineva, L. Stievano, E. Fonda, F. Jaouen, *Nat. Mater.* **2015**, *14*, 937.

[23] I. Martinaiou, A. H. A. Monteverde Videla, N. Weidler, M. Kübler, W. D. Z. Wallace, S. Paul, S. Wagner, A. Shahraei, R. W. Stark, S. Specchia, U. I. Kramm, *Appl. Catal. B* **2020**, *262*.

[24] L. Liu, G. Zeng, J. Chen, L. Bi, L. Dai, Z. Wen, *Nano Energy* **2018**, *49*, 393.

[25] L. Lin, Q. Zhu, A. W. Xu, *J. Am. Chem. Soc.* **2014**, *136*, 11027.

[26] D. Liu, J.-C. Li, Q. Shi, S. Feng, Z. Lyu, S. Ding, L. Hao, Q. Zhang, C. Wang, M. Xu, T. Li, E. Sarnello, D. Du, Y. Lin, *ACS Appl. Mater. Interfaces* **2019**, *11*, 39820.

[27] X. Cui, S. Yang, X. Yan, J. Leng, S. Shuang, P. M. Ajayan, Z. Zhang, *Adv. Funct. Mater.* **2016**, *26*, 5708.

[28] Y. Qian, T. An, K. E. Birgersson, Z. Liu, D. Zhao, *Small* **2018**, 1704169.

[29] Z. Lyu, S. Ding, M. Wang, X. Pan, Z. Feng, H. Tian, C. Zhu, D. Du, Y. Lin, *Nanomicro. Lett.* **2021**, *13*, 146.

[30] S. Lu, M. Hummel, Z. Gu, Y. Wang, K. Wang, R. Pathak, Y. Zhou, H. Jia, X. Qi, X. Zhao, B. B. Xu, X. Liu, *ACS Sustainable Chem. Eng.* **2021**, *9*, 1703.

[31] X. Liang, Z. Li, H. Xiao, T. Zhang, P. Xu, H. Zhang, Q. Gao, L. Zheng, *Chem. Mater.* **2021**, *33*, 5542.

[32] T. Marshall-Roth, N. J. Libretto, A. T. Wrobel, K. J. Anderton, M. L. Pegis, N. D. Ricke, T. V. Voorhis, J. T. Miller, Y. Surendranath, *Nat. Commun.* **2020**, *11*, 5283.

[33] Z. Lyu, S. Ding, N. Zhang, Y. Zhou, N. Cheng, M. Wang, M. Xu, Z. Feng, X. Niu, Y. Cheng, C. Zhang, D. Du, Y. Lin, *Research* **2020**, *2020*, 4724505.

[34] H. Gharibi, N. Dalir, M. Jafari, M. J. Parnian, M. Zhiani, *Appl. Surf. Sci.* **2022**, *572*.

[35] J. Han, H. Bao, J.-Q. Wang, L. Zheng, S. Sun, Z. L. Wang, C. Sun, *Appl. Catal. B* **2021**, *280*.

[36] X. Wei, X. Luo, H. Wang, W. Gu, W. Cai, Y. Lin, C. Zhu, *Appl. Catal. B* **2020**, *263*.

[37] S. Akula, M. Mooste, B. Zulevi, S. McKinney, A. Kikas, H.-M. Piirsoo, A. Tamm, V. Kisand, A. Serov, E. B. Creel, D. A. Cullen, K. C. Neyerlin, H. Wang, M. Odgaard, T. Reshetenko, K. Tammeveski, *J. Power Sources* **2022**, *520*, 230819.

[38] Y. Li, W. Zhou, H. Wang, L. Xie, Y. Liang, F. Wei, J.-C. Idrobo, *Nat. Nanotechnol.* **2012**, *7*, 394.

[39] J. Liang, X. Du, C. Gibson, X. W. Du, S. Z. Qiao, *Adv. Mater.* **2013**, *25*, 6226.

[40] Y. Wang, H. Lei, H. Xiang, Y. Fu, C. Xu, Y. Jiang, B. B. Xu, E. H. Yu, *Adv. Energy Sustainability Res.* **2021**, *2*, 2100083.

2200276 (7 of 7)